Supplementary Materials

List of the Supplementary Materials

      Materials and Methods

      Figures S1-S11

      Captions for Movies S1-S10

Materials and Methods

Xenopus laevis **egg extracts.** Interphase-arrested extracts were prepared following the protocol of Deming and Kornbluth (*10*), except that the ATP-regenerating system was not added. If the extract appeared excessively turbid or contained a large amount of debris, a low speed clarifying spin similar to that described by Murray (*12*) was performed to remove excessive debris from the extract. For small volumes of extract, 0.4 ml snap-cap microtubes (485050, E&K Scientific) were used for clarifying and were centrifuged at 4°C for 5 min in a Beckman Microfuge E with a horizontal rotor. The top lipid and bottom dark debris layers were cut off with a clean razor blade and the remaining volume recovered. For larger volumes, 1.5 ml Eppendorf microcentrifuge tubes were used for an 8 min spin (4°C, 12000 g) in a tabletop Eppendorf centrifuge, and extracts were recovered with a wide-bore pipette tip. Care was taken to recover all accessible volume except the debris located at the top and bottom of the tube after the spin. In the experiments described in figure S11, extracts were diluted with freshly-prepared egg lysis buffer (pH 7.7, 250 mM sucrose, 10 mM HEPES, 50 mM KCl, 2.5 mM $MgCl_2$, 1 mM DTT). Cell cycle extracts were prepared following Murray (*12*), with the modifications that eggs were activated by treatment with 0.5 µg/ml calcium ionophore A23187 (C7522, MilliporeSigma) and that energy mix was not added. As noted in the text, in some experiments we omitted the actin-depolymerizing agent cytochalasin B from the standard extract preparations, or substituted latrunculin A (10 µM) for cytochalasin B.

Demembranated sperm nuclei and nuclear markers. Demembranated *Xenopus laevis* sperm nuclei were prepared as described by Murray (*12*). For all experiments the final concentration of demembranated sperm nuclei in the extract was 160 nuclei/µl, except for the experiment in Fig. 1D and figure S1A, which was 27 nuclei/µl, figure S1B experiment #2, which was 80 nuclei/µl, and the experiment in Fig. 2D, for which the final concentrations are indicated at the top of each panel. The nuclear markers used were fusion proteins consisting of glutathione-S-transferase, green fluorescent protein, and a nuclear localization sequence (GST-GFP-NLS) or GST-mCherry-NLS, expressed in *E. coli* and purified by Jeremy Chang (*17, 18*), and referred to in the text as GFP-NLS and mCherry-NLS for brevity. For Fig. 1D, figure S1A, and figure S8 GFP-NLS was used as the nuclear marker, and the final concentration in the extracts was approximately 0.38 µM. For the rest of the experiments, mCherry-NLS was used as the nuclear marker, and the final concentration in the extracts was approximately 0.35 µM, except for the experiment described in figure S11, for which the final concentration was approximately 0.7 µM.

Microtubule and F-actin markers. Fluorescently-labeled tubulin (TL670M-A and TL488M-A, Cytoskeleton, Inc.) was dissolved in water as a 200 µM stock solution, held on ice, and used within 30 min. The final concentration in extracts was 1 µM for all experiments. In movie S1 and S2, HiLyte 488 labeled tubulin from porcine brain (TL488M-A, Cytoskeleton, Inc.) was used as the microtubule marker. For all other labeled-tubulin experiments, HiLyte 647 labeled tubulin from porcine brain (TL670M-A, Cytoskeleton, Inc.) was used.

SiR-tubulin (CY-SC002, Cytoskeleton, Inc.) was used in the confocal experiments as indicated in the figures, figure legends and text. The final concentration of SiR-tubulin in the experiment presented in Fig. 1E, Fig. 2C, figure S2, figure S5, was 200 nM.

SiR-actin (CY-SC001, Cytoskeleton, Inc.) was used to detect F-actin in the experiments as indicated in the figures and text. The final concentration of SiR-actin ranged from 200 nM to 1 µM.

Other fluorescent markers. Fluorescent ER-Tracker dyes (ThermoFisher) were used to visualize the ER. All fluorescent ER markers were used at a final concentration of 1 µM. ER-Tracker Red (E34250, ThermoFisher) was used in Fig. 1D, figure S1A, figure S1B experiment #2, movies S1, S2 and S3, and in the blebbistatin experiments (Table 1). ER-Tracker Green (E34251, ThermoFisher) was used in all other experiments. MitoTracker Red CMXRos (M7512, ThermoFisher) was used to visualize mitochondria at a final concentration of 500 nM. CellMask™ Green Plasma Membrane Stain (C37608, ThermoFisher) was used at a final concentration of 5 µg/ml. DNA was stained by Hoechst 33342 (H3570, ThermoFisher), used in extracts at a final concentration of 5 µg/ml.

Imaging chambers. Fluorinated ethylene propylene tapes (23-FEP-2-5, CS Hyde Company) were used to mask glass coverslips (260365, Ted Pella, Inc.) to make the imaging chambers. Imaging spacers with a 120 µm depth (70327-8S, Electron Microscopy Sciences) were used to provide support for the chambers. The experiment shown in Fig. 4B was carried out in a non-tissue-culture-treated bacteriological Petri dish (351007, Corning). The cycling extract was gently laid on the dish surface as a thin disk-shaped layer about 1 mm in diameter with a pipette tip and immediately covered with mineral oil (330760, MilliporeSigma). All other imaging was done using the FEP-clad coverslips.

Inhibitors. Nocodazole (M1404), ciliobrevin D (250401), cytochalasin B (C6762), (+)-S-trityl-L-cysteine (164739), and (−)-blebbistatin (B0560) were from MilliporeSigma. Apyrase (M0398S) was from New England BioLabs. Latrunculin A (ab144290) was from Abcam. TC-S 7010 (S1451), GSK923295 (S7090), ispinesib (S1452), SB743921 HCl (S2182), volasertib (S2235), and BI 2536 (S1109) were from Selleck Chemicals. For experiments shown in figure S7, the inhibitors BI 2536 and volasertib were added to the extracts prior to adding demembranated sperm nuclei. In imaging extracts supplemented with (−)-blebbistatin, care was taken to minimize light exposure during transport to the microscope, and imaging was done with excitation wavelengths longer than blue light (488 nm) to avoid photoinactivation of the inhibitor. Inhibitors were used at final concentrations indicated in Table 1.

Imaging and analysis. All epifluorescence imaging was carried out at room temperature on a Leica DMi8 inverted epifluorescence microscope with a 5x air objective and a Hamamatsu Orca

Flash LT sCMOS camera. All confocal imaging was carried out at room temperature on a Nikon Eclipse-TI inverted microscope with a PLAN APO 20x 0.75 N.A. air objective and a Photometrics Prime95B sCMOS camera controlled with NiS-Elements software.

Extract samples were held on ice prior to commencing time lapse microscopy, and imaging typically began 5 to 10 min after the samples were taken off ice.

The confocal images were corrected for uneven illumination using the BaSiC tool (*19*). Both dark-field and flat-field shading were estimated and used for correction. The regularization parameters for both shading models were set to 2. To obtain a large enough field of view for characterizing compartment formation, image tiles acquired by the 20x objective were stitched together by a custom MATLAB script. Regions of interest were then selected for display.

Care was taken to set the displayed range of fluorescence intensities identically for each channel in comparable images; e.g., for different time points in a time course, or for ± drug images in an endpoint experiment.

The spatial fluorescence intensity profiles in Fig. 1F were calculated by line-scan analysis. Images from the 1 h time point were used for this analysis. For each experiment, images with the same field of view from each fluorescence channel were selected for line-scan analysis. The line scan was performed using the line tool in Fiji/imageJ and the Plot Profile function. The fluorescence intensity was extracted along a 15-pixel thick line segment that began in the border zone, went through the center of the compartment (where the nuclei are), and ended in the border zone on the opposite side of the compartment. The extracted intensities for each channel were then normalized within the same experiment. The intensity profiles associated with each compartment from multiple experiments were center-aligned by their nuclear fluorescence peak. Intensity values from the same fluorescence channel across experiments at each spatial location were used to compute the average intensity and the interdecile range, which included 80% of the data points at that location.

The effect of incubation time on border width presented in Fig. 1G, left, was calculated as follows. For the correlation between incubation time and border width, the same 9 compartments were analyzed at different points in time. The peripheral edges of each compartment were determined by image segmentation based on ER or tubulin fluorescence signal using a custom MATLAB script. Here the area of a compartment was defined as the area enclosed by these edge points. To determine the border width associated with a compartment that had n edge points, the shortest distance between each of its edge points and the edge points of its neighboring compartments d_i ($i = 1, 2, \ldots, n$) was determined. The border width associated with the compartment was the average of d_i. The data used for the microtubule compartment area vs. border width plot (Fig. 1G, right) were calculated similarly, but only from extracts that had reached a stable size, which was taken as 42 min for the extracts with sperm and 100 min for the extracts without sperm.

To estimate the overall area occupied by the border zones, tubulin fluorescence images from 6 separate experiments with nucleated compartments at the 1 h time point were analyzed. The compartment regions were segmented using data from the tubulin channel and the inverted image was used to estimate the percentage of the area occupied by the border zones.

The areas of the cell-like compartments in Fig. 2E were calculated as follows. The compartments were identified by image segmentation based on the fluorescent tubulin signal. Here we wanted to calculate the domain area the compartments occupied, which was defined by the area enclosed by the curve that evenly divided the space between the tubulin-positive region of the compartment and that of its immediately neighboring compartments. Compartments that were on the edge of the image, poorly formed, or only partially visible, were not counted. The segmentation results were re-checked manually and corrections were made when necessary. Note that the compartment area calculated here included not only the tubulin-spanned domain, but also the parts of the border zone that were associated with the compartment.
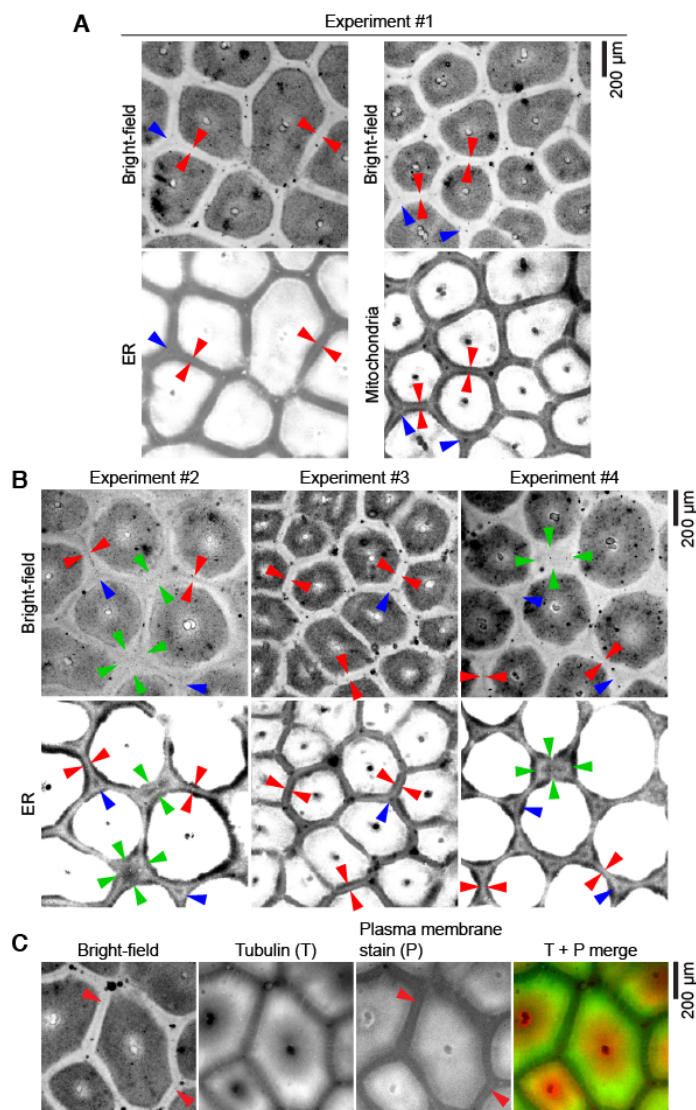
Figure S1. Examples of the border region between neighboring cell-like compartments.

(A) Bright-field and fluorescence images from the same experiment as Fig. 1D, showing the details of the border region between neighboring cell-like compartments. The mid-border regions stained with ER-Tracker and MitoTracker. **(B)** Examples from three independent experiments showing the border region between cell-like compartments. In each panel of the figure, pairs of red arrowheads indicate a boundary between two compartments. Each blue arrowhead indicates a junction where boundaries of three compartments meet. Green arrowheads indicate disjoint boundaries. For each fluorescence image, the arrowheads are placed at the same locations as in the corresponding bright-field image. The brightness and contrast of fluorescence images have been linearly adjusted to allow the boundary features to be appreciated. ER, endoplasmic reticulum. **(C)** Plasma membrane staining. An amphipathic plasma membrane probe (CellMask^TM) stained the compartments as well as the mid-border structures (red arrowheads) observed by bright-field microscopy. In the merged image, tubulin is shown in green and plasma membrane stain in red. Related to Fig. 1.
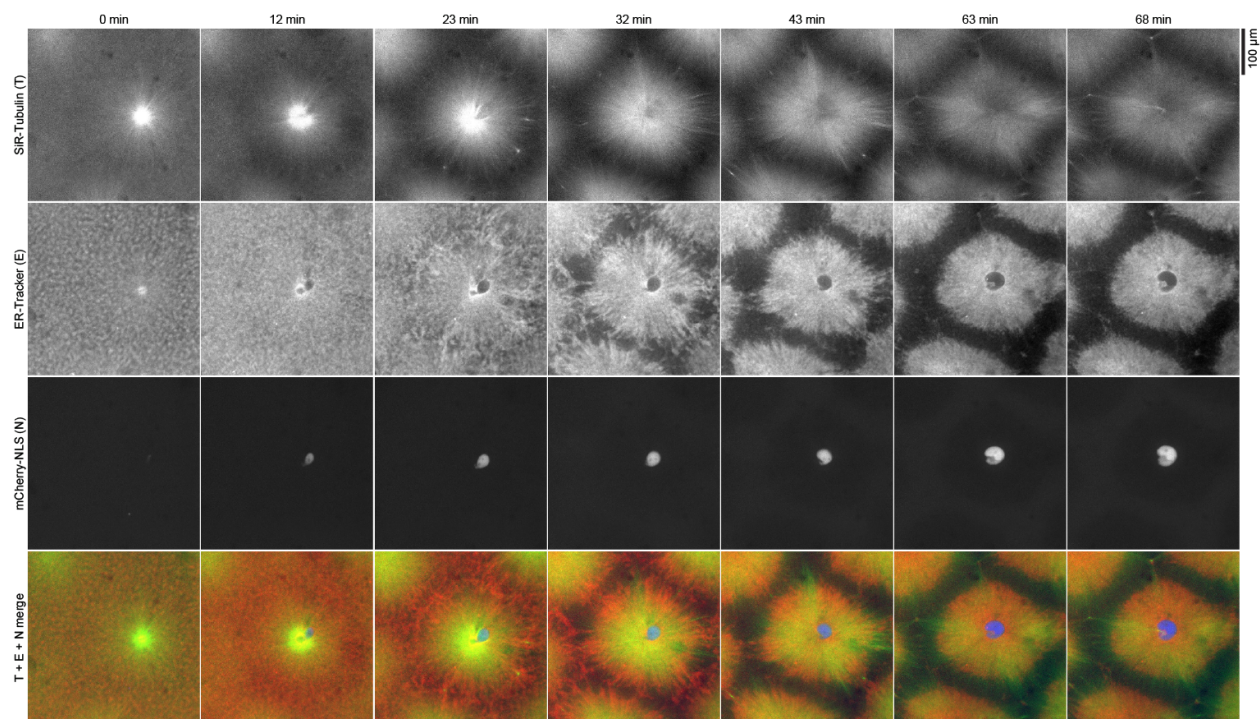
Figure S2. Confocal microscopy time course of compartment formation in an interphase extract with added sperm nuclei.

Initially, there was a prominent microtubule aster and the ER had a characteristic texture. At 12 min, microtubules at the periphery of the aster began to be depleted. By 23 min, microtubule junctional complexes had emerged as bright foci at the periphery of the aster, where the microtubules were otherwise noticeably depleted. The texture of ER in the microtubule-depleted region further coarsened and distinct compartments began to form. By 32 min, the ER of each compartment had separated further from neighbors, and the microtubule junctional complexes persisted. The mature pattern formed at 63-68 min, with several junctional complexes visible in the microtubule and ER channels at the corners where compartments met. In the multi-color merge panels, SiR-tubulin signal is shown in green, ER-Tracker in red, and the mCherry-NLS in blue. Images are maximum intensity projections from 5 confocal z-slices 10 μm apart. The data are from the same experiment as that described in Fig. 1E.
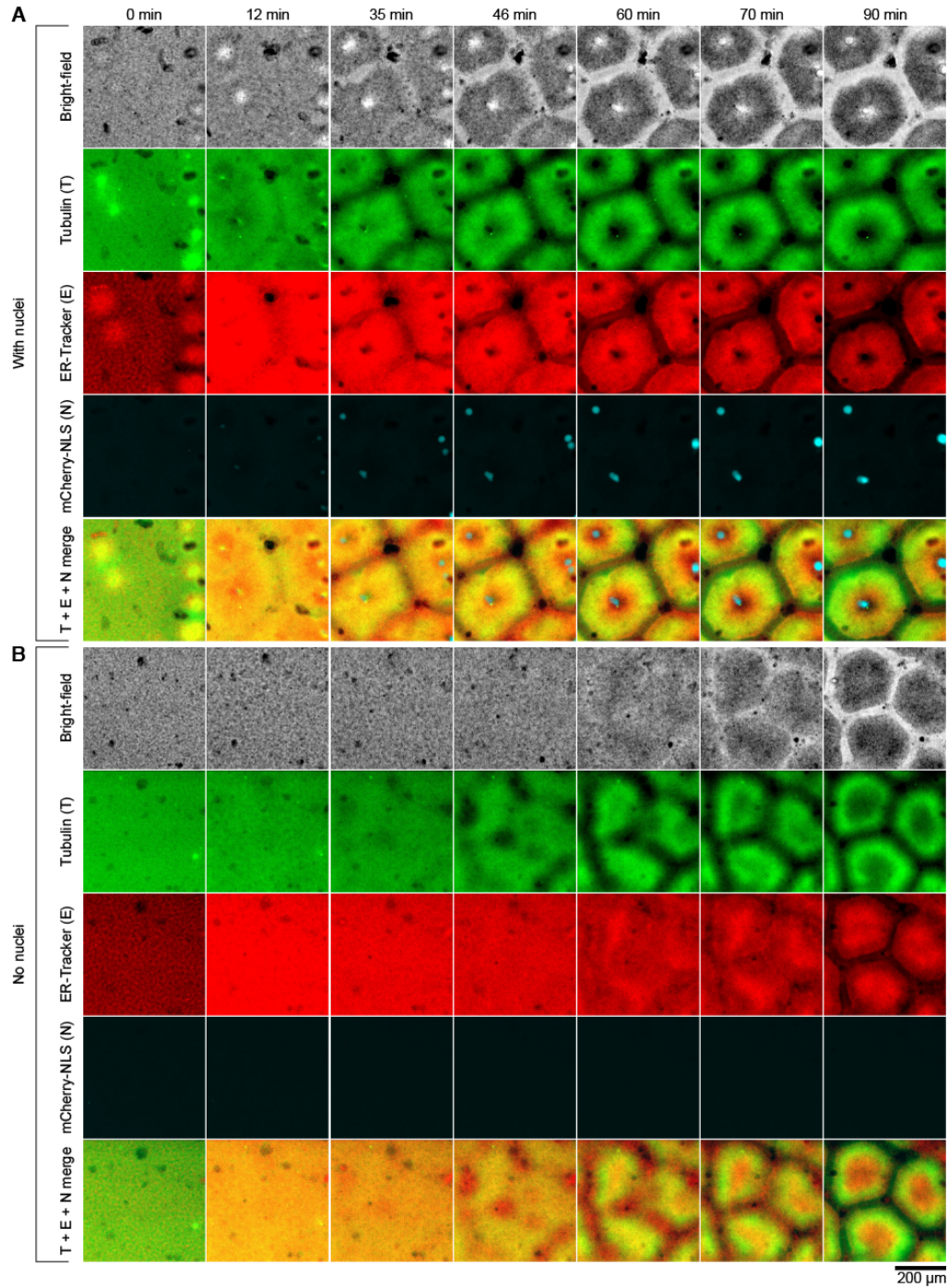
Figure S3. The formation of cell-like compartments does not require added demembranated sperm nuclei.

(A) Time lapse montage of cell-like compartment formation in an interphase egg extract with approximately 160 demembranated *Xenopus laevis* sperm nuclei added per microliter of extract. **(B)** Time lapse of compartment formation in an extract from the same experiment as (A) but with no sperm nuclei added. (A) and (B) share the scale bar located at the bottom of (B). Related to Fig. 2A, B.
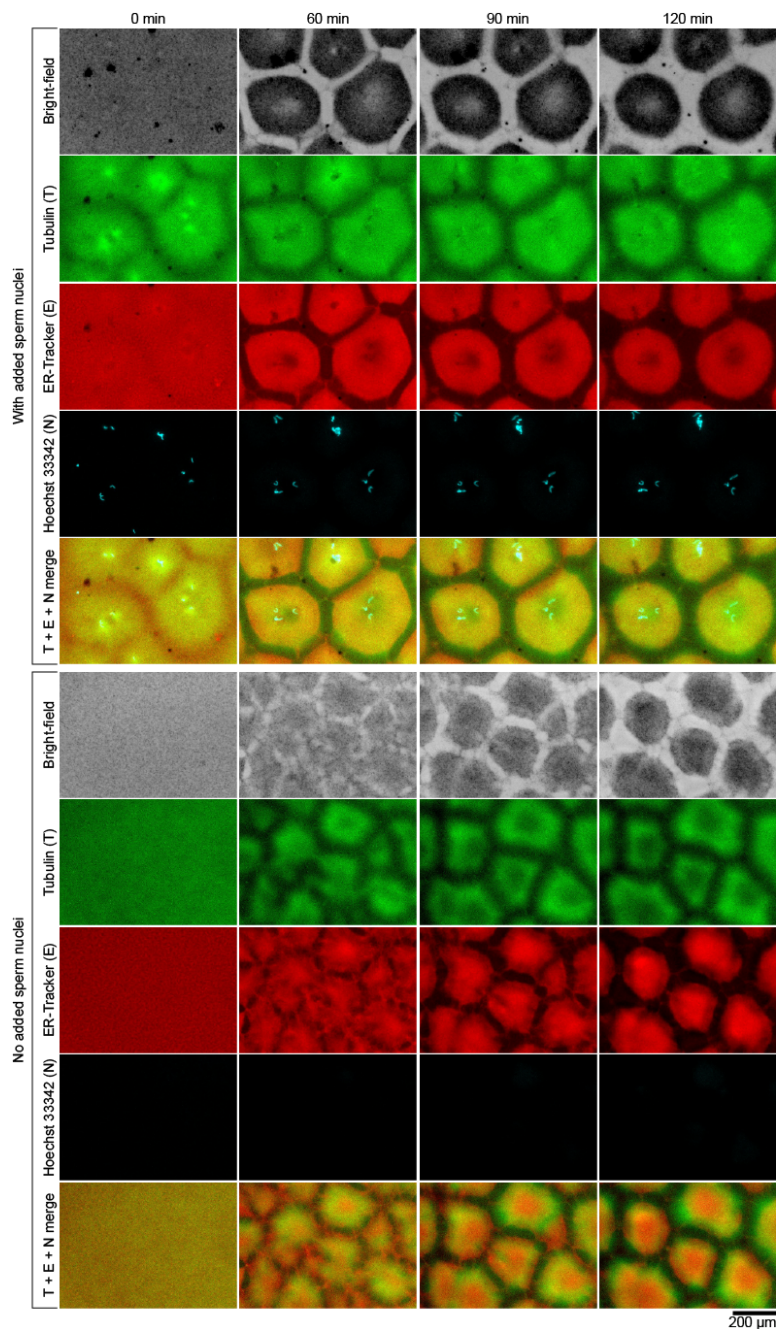
Figure S4. Cell-like compartment formation is normal in the absence of DNA.

Time lapse images of pattern formation in interphase-arrested egg extracts with and without added sperm nuclei. DNA was detected with Hoechst 33342 (5 µg/ml). Compartments formed normally in both cases. In the extract with added sperm nuclei, strong DNA staining was observed from the beginning of the time course, and persisted until the end. In the extract with no added sperm, there was no detectable DNA staining. Note that when Hoechst 33342 was used to stain the DNA in the sperm chromatin, the sperm nuclei would typically retain their worm-like morphology for the duration of pattern formation process. Related to Fig. 2.
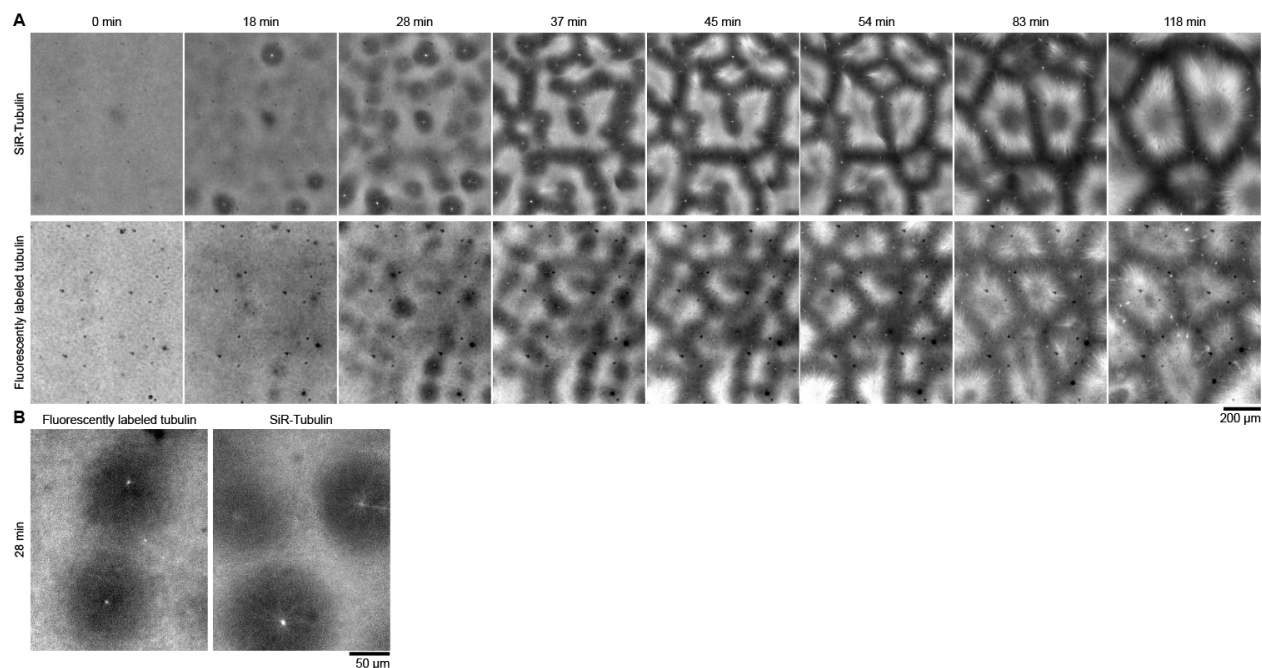
Figure S5. SiR-tubulin and fluorescently labeled tubulin report the same features and dynamics of microtubule organization in extracts with no added sperm.

(A) Detailed confocal time course of microtubule dynamics during compartment formation in extracts without added sperm nuclei. The top row shows an experiment where SiR-tubulin was used to visualize microtubules, and the bottom row shows a separate experiment where HiLyte 647 labeled tubulin was used to visualize microtubules. The dynamics and appearance of microtubule patterns were very similar in these two cases, indicating the binding-based microtubule probe SiR-tubulin did not introduce artifacts in compartment formation. (B) Magnified view of microtubule foci at the centers of microtubule-depleted zones during early stages of pattern formation. The phenomenon reported by SiR-tubulin is very similar to that reported by HiLyte 647 labeled tubulin. Images are maximum intensity projections from 5 z-slices 10 μm apart. Related to Fig. 2C.
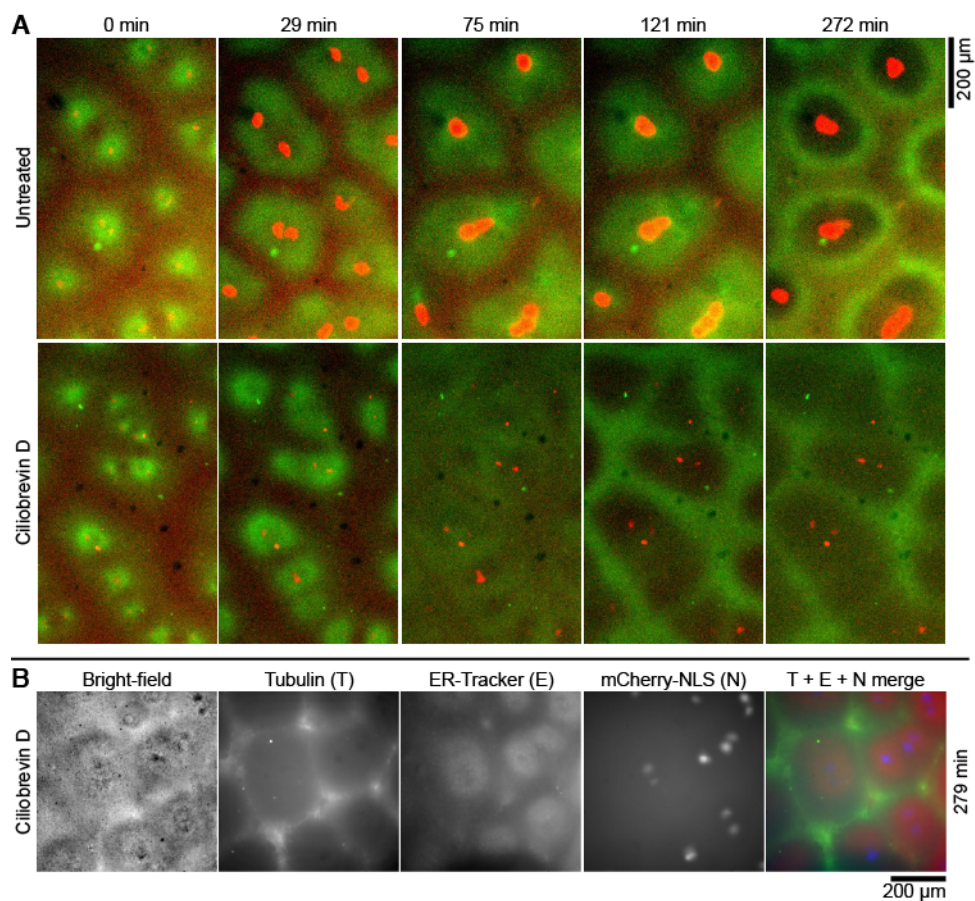
Figure S6. Effect of the cytoplasmic dynein inhibitor ciliobrevin D on pattern formation.

(A) Time lapse images showing microtubule and nuclear dynamics in control and ciliobrevin D-treated extracts. Tubulin (green) and mCherry-NLS (red) were visualized by 5x epifluorescence microscopy. In the ciliobrevin D-treated sample, the mCherry-NLS signal has been boosted to allow the poorly-formed nuclei to be visible. Note that in the drug-treated extract, the fluorescently-labeled tubulin adopted a abnormal localization by 121 min, and the nuclei never became properly centered. **(B)** Higher magnification (20x) view of the final pattern in a ciliobrevin D-treated extract, revealing fiber-like texture of microtubules accumulated in the border zone, and mislocalized nuclei. In the T + E + N merge panel, tubulin is shown in green, ER in red, and mCherry-NLS in blue. Related to Fig. 3B.
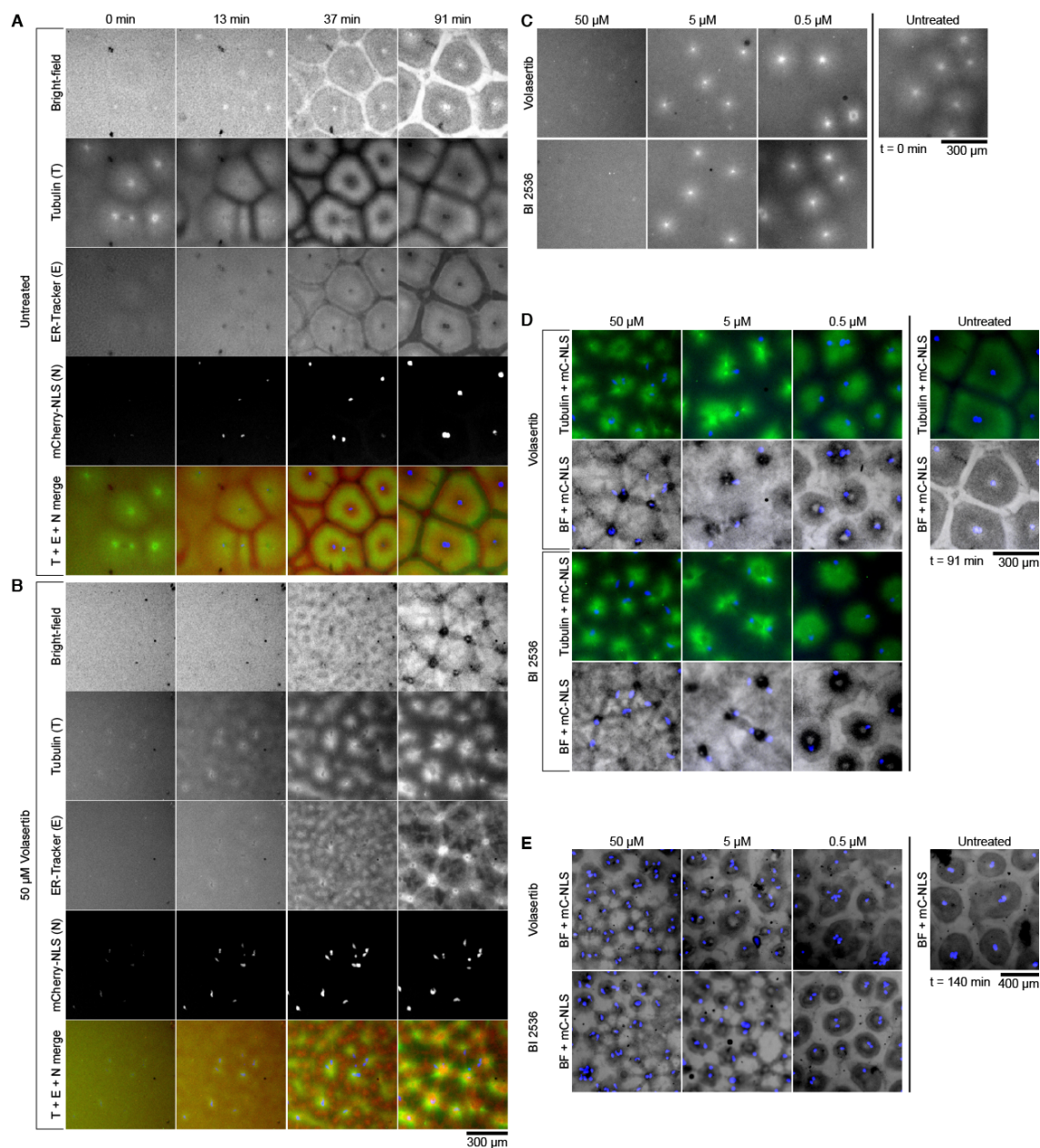
Figure S7. Effect of Plk1 inhibitors on pattern formation.

(A, B) Time course of pattern formation in a control extract (A) and an extract treated with a maximal (50 μM) concentration of the Plk1 inhibitor volasertib (B). Note that in the drug-treated extract there were no visible asters, the nuclei were mislocalized, and the ER adopted an abnormal web-like geometry. (A) and (B) share the same scale bar located at the bottom of (B). **(C)** Dose-dependence of the abnormal aster phenotype in extracts treated with volasertib and BI 2536, a second Plk1 inhibitor. Shown are microtubule images reported by fluorescently labeled tubulin. **(D)** Dose-dependence of the abnormal nuclear centering and ER morphology in extracts treated with volasertib or BI 2536. **(E)** A variation in the overall patterning phenotype from a separate experiment. In all merged images, if present, tubulin is shown in green, ER in red, and mCherry-NLS in blue. mC-NLS, mCherry-NLS. Related to Table 1.
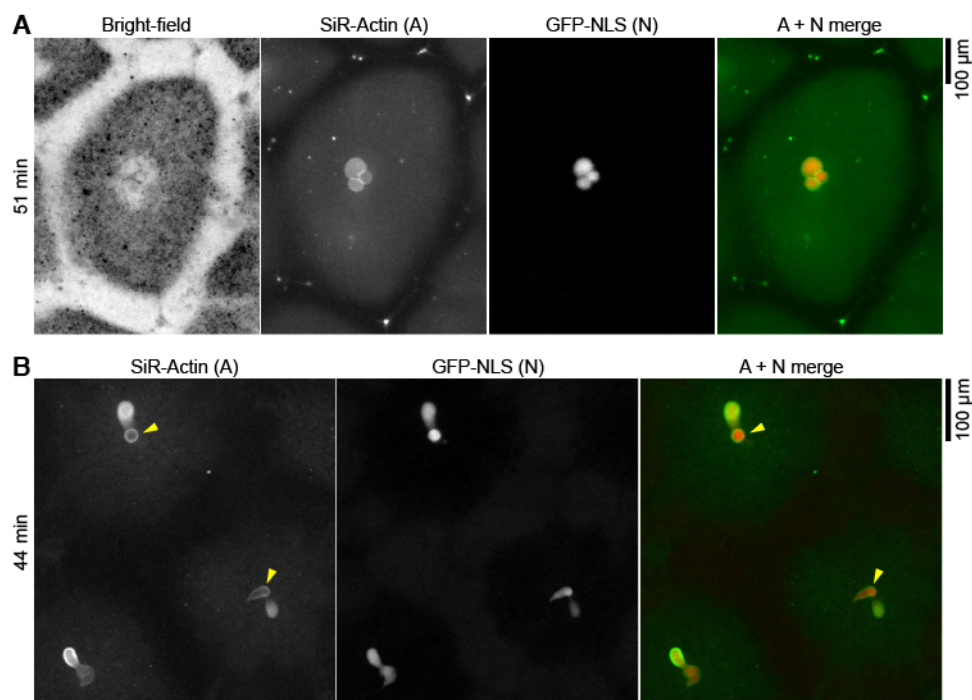
Figure S8. Perinuclear localization of F-actin in extracts prepared in the absence of the actin polymerization inhibitor cytochalasin B.

(A) Bright-field and epifluorescence images showing the localization of F-actin (reported by SiR-actin) relative to the nuclei (reported by GFP-NLS). **(B)** Confocal images from a single z-slice. Arrowheads indicate particularly clear examples of actin perinuclear localization. In both epifluorescence and confocal merge panels, SiR-actin stain is shown in green and GFP-NLS signal is shown in red. Related to Fig. 3C.
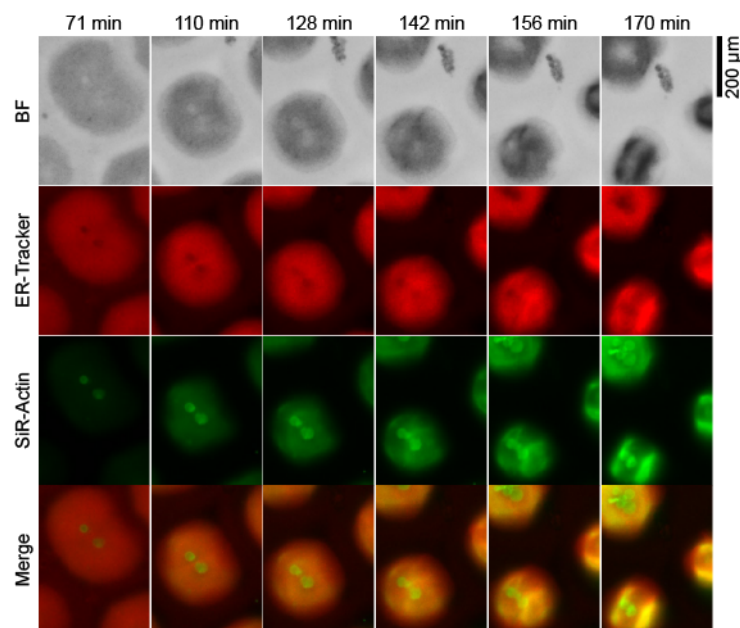
Figure S9. An example of an actin-intact compartment that shrank and rolled.

Time lapse images of bright-field, ER-Tracker and SiR-actin stain corresponding to the actin images shown in Fig. 3E. The actin channel showed a cage-like structure that surrounded the two nuclei. The top and bottom of the cage seen at the 170 min time point were ~120 µm apart, which was the thickness of the spacer that separated the cover slips. Related to Fig. 3E.
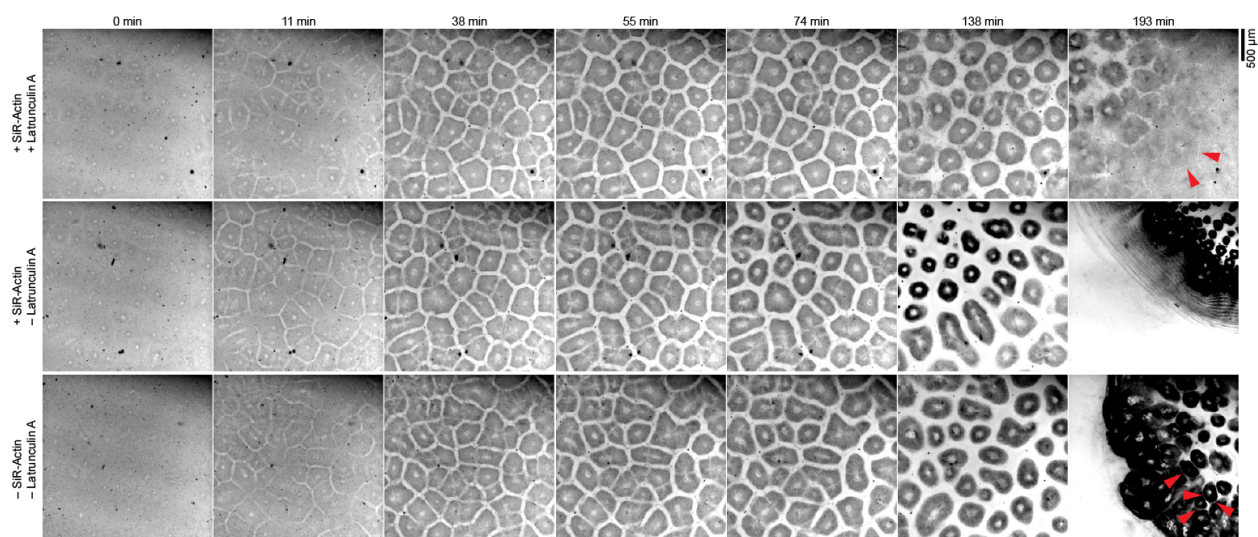
Figure S10. Neither latrunculin A nor SiR-actin affects the initial stages of pattern formation.

Time lapse montage of bright-field images of compartment formation in interphase extracts under various conditions. The presence of the F-actin probe SiR-actin (1 µM) did not affect the timing of compartment formation or the appearance of the compartments, and the extracts underwent the late stage contraction expected of actin-intact extracts (compare the middle row and the bottom row). The presence of the actin polymerization inhibitor latrunculin A also had no effect on the timing of compartment formation or the appearance of the compartments (compare the top row and the middle row), and it inhibited the late stage contraction seen in actin-intact extracts (193 min, top panel). Note that even after the extract became apoptotic (193 min, top panel) or contracted (193 min, middle and lower panels), distinct compartments persisted (red arrowheads). Related to Fig. 3C through E.

15
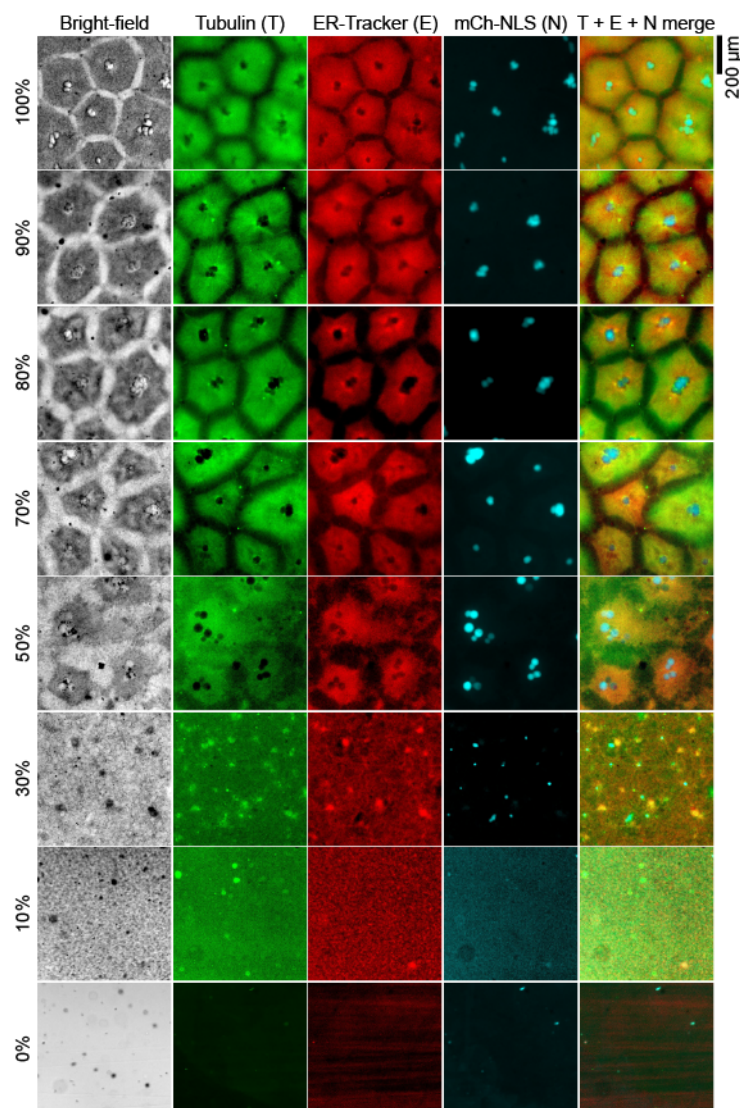
Figure S11. The effect of dilution on pattern formation.

Undiluted interphase extracts were mixed with various amounts of egg lysis buffer as indicated. Sperm nuclei, fluorescently labeled tubulin, ER-Tracker and mCherry-NLS were added after the indicated dilutions; thus the final concentrations of these probes were the same across all extracts. mCh-NLS indicates mCherry-NLS.

Movie Captions

Movie S1. Homogenized *Xenopus laevis* egg extracts self-organize into cell-like compartments.

Time lapse video of bright-field, tubulin, ER and tubulin-ER overlay channels of cell-like compartment formation dynamics in interphase *Xenopus laevis* egg extracts. Related to Fig. 1C.

Movie S2. Detailed view of spontaneous cell-like compartment formation in *Xenopus laevis* egg extracts.

Time lapse video of bright-field, tubulin, ER and tubulin-ER overlay channels of cell-like compartment formation dynamics in interphase *Xenopus laevis* egg extracts, focusing on a small region of the imaging field to reveal more details. The migration of nuclei from their initial locations during the compartment formation process is readily visible, indicating that the initial localization of added demembranated sperm nuclei does not entirely determine the final pattern of the compartments. Related to Fig. 1C.

Movie S3. The organization of microtubules, endoplasmic reticulum, mitochondria and the nucleus in the cell-like compartment resembles that of a typical cell.

Time lapse video of bright-field, tubulin, mitochondrial, ER, nuclear and overlay channels of cell-like compartment formation dynamics in interphase *Xenopus laevis* egg extracts. Related to Fig. 1D.

Movie S4. The formation of cell-like compartments in egg extracts does not require added demembranated sperm nuclei.

Time lapse video of bright-field, tubulin, ER, nuclear and overlay channels of cell-like compartment formation dynamics in interphase *Xenopus laevis* egg extracts with added demembranated sperm nuclei (top panels) and without added nuclei (bottom panels). Related to Fig. 2A and B.

Movie S5. Confocal view of the formation of cell-like compartments with and without added demembranated sperm nuclei.

Time lapse video of confocal images of SiR-tubulin, ER, and nuclei during pattern formation in extracts. In the merge panels, SiR-tubulin is green, ER is, and nuclei are blue. Images are maximum intensity projections from 5 z-slices 10 μm apart. Related to Fig. 1E and Fig. 2C.

Movie S6. Cell-like compartment patterns in extracts with different concentrations of added demembranated sperm nuclei.

Time lapse video of cell-like compartment formation in interphase *Xenopus laevis* egg extracts supplemented with different concentrations of demembranated sperm nuclei. Related to Fig. 2D.

Movie S7. Formation of cell-like compartments requires microtubule polymerization.

Time lapse video of cell-like compartment formation in interphase *Xenopus laevis* egg extracts without nocodazole treatment (top panels) and with 33 μM nocodazole treatment (bottom panels). Related to Fig. 3A and Table 1.

Movie S8. Effect of the cytoplasmic dynein inhibitor ciliobrevin D on the formation of cell-like compartments.

Time lapse video of a normal extract (top) and an extract treated with ciliobrevin D (50 μM). Related to Fig. 3B and Table 1. Note that the microtubules initially concentrated in central asters and then flipped to the periphery at ~70 min.

Movie S9. The cell-like compartment is capable of mitotic division.

Time lapse video of a sperm-supplemented cycling *Xenopus laevis* egg extract. Note that a cell-like compartment formed in the first interphase after meiotic exit by dynamics similar to those observed in interphase-arrested extracts. This compartment subsequently entered mitosis and gave rise to two daughter compartments. Related to Fig. 4A.

Movie S10. The cell-like compartment can perform multiple cycles of division and reorganization.

Time lapse video of a sperm-supplemented cycling *Xenopus laevis* egg extract undergoing five successive cycles of division. Epifluorescence of mCherry-NLS (red), which accumulates in interphase nuclei, is superimposed on bright-field images.